Journal of Sound and Vibration (1999) **222**(4), 579–596
Article No. jsvi.1998.2068, available online at http://www.idealibrary.com on IDEAL

THE INFLUENCE OF LUBRICATION ON THE DYNAMIC BEHAVIOUR OF BALL BEARINGS

Y. H. WIJNANT,[†] J. A. WENSING,[†,‡] G. C. VAN NIJEN[‡]
[†]*University of Twente, Enschede, The Netherlands*
[‡]*SKF Engineering & Research Center, Nieuwegein, The Netherlands*

(*Received* 19 *February* 1998, *and in final form* 13 *November* 1998)

Investigation into the dynamic behaviour of rolling element bearings is motivated by the urge to reduce vibrations in rolling bearing applications. The dynamics of the bearing is governed by both the dynamics of its structural elements, i.e., the inner ring, the outer ring and the rolling elements, and the elastohydrodynamic lubricated (EHL) contacts connecting these structural elements. To investigate the effect of the lubricant on the dynamic behaviour of deep groove ball bearings, computational models have been developed for both the EHL problem and the structural dynamics problem. In the present study, the interaction between the structural elements is described by means of a non-linear spring-damper model which is based on numerical solutions of the full EHL contact problem. These relations have subsequently been adopted in the structural dynamics bearing model. Using these models, the shift of bearing eigenfrequencies as a result of lubrication is investigated and modal damping values for the preloaded bearing are estimated. It is suggested that the shift of the eigenfrequencies is mainly caused by contact angle variations.

1. INTRODUCTION

Nowadays load capacity and life time of rolling bearings have become less critical for certain applications in the car and household industry. Here, bearing quality is increasingly determined by its acoustical or vibrational performance, mainly driven by severe governmental regulations and customer demands. The importance with respect to the vibrational behaviour is explained by the fact that bearings are always in the transmission path of vibrations between the shaft and the bearing housing. The determination of the transmission of vibrations over a rolling bearing requires solving the equations that govern the dynamics of the structural components and the EHL contacts connecting them. However, nowadays computer capacity is still far from solving the equations simultaneously. Therefore, in the present study, these problems have been solved separately, i.e., relations based on numerical results of a *single* EHL contact model have been incorporated into a structural bearing model.

In EHL theory, it is generally assumed that the rolling element is subjected to a constant load. Entraining motion then causes the build up of pressure which

0022–460X/99/190579 + 18 $30.00/0

results in a contact force, i.e., the integral over the pressure, which is normally required to equal the applied load. This is sufficient when studying the stifiness of the smooth EHL contact and only when studying the influence of surface features like roughness or waviness is a transient analysis required, see e.g., references [1–3]. However, when studying the interaction of structural vibrations and the fluid film the model should somehow be time-dependent and both squeeze as well as entraining motion should be taken into account. To the authors' knowledge, no studies of the full EHL contact problem exist which focuses on the stiffness and damping, but related topics were investigated by e.g., Yang and Weng [4], Larsson [5] and Dowson and Wang [6]. A preliminary study on fluid–structure interaction in an EHL circular contact, including squeeze and entraining motion as well as inertia forces was reported in Wijnant and Venner [7]. In this study, both a dry and lubricated contact were examined. For two particular examples it shows that the lubricant damps rolling element vibrations that result from a small initial deviation from equilibrium. Furthermore, it is shown that any oscillation of the roller induces film thickness modulations whose wavelength is related to the roller's oscillating frequency in a dry contact situation.

In this paper focus will be on stiffness and damping of the EHL contacts. The stiffness has been accurately determined from steady state numerical solutions for both circular and elliptical contacts. Damping values for the circular contact have been obtained by fitting numerical solutions of the full EHL problem to the solutions of a simplified spring–damper model. Unfortunately, despite the second order discretization and the fine mesh that was used, the calculated damping values are still dominated by the discretization error for small ellipticity ratio's.

The dynamics of the structural elements of the bearing is described by a set of non-linear equations of motion, with time-dependent coefficients. Physical non-linearities are introduced by the ball raceway contacts. Apart from the fact that rolling elements can suffer from loss of contact, the contacts themselves, as can be concluded from the EHL analysis, behave as stiffening springs. In case of large contact angle variations, the bearing system also contains geometric non-linearities (pendulum effect). The time-dependency of the coefficients is caused by the finite number of rotating rolling elements. The periodically varying coefficients give rise to parametrically excited vibrations, which again can cause unstable behaviour of the bearing.

Rolling bearings are also known for their complex vibration generation mechanisms. A number of important sources of vibration are out-of-roundness, roughness, defects and dirt. In the production environment, standard tests exist for detecting these excitation mechanisms. In this test, see Figure 1, the bearing is mounted on a spindle rotating at a fixed speed. The outer ring is loaded with a pure axial force. The numerical examples in this paper are inspired by this particular test.

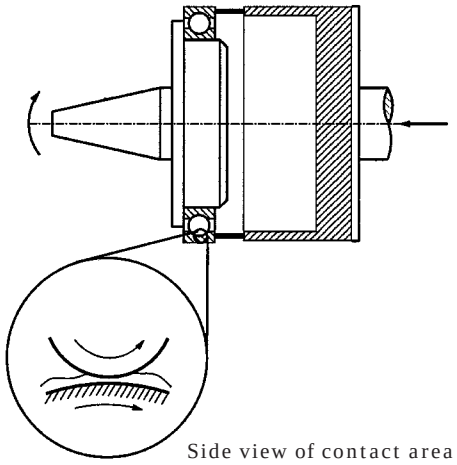

Figure 1. Test apparatus for rolling bearings.

2. THE EHL CONTACT MODEL

Consider a rolling element running on a lubricated raceway of a rolling bearing, as given in Figure 2. Due to the applied load, both the rolling element and the raceway will deform elastically and remote points beneath the surfaces will approach each other. This approach, denoted by δ in Figure 2, as a function of the applied load is the flexibility of the contact. The stiffness, which will be referred to as the EHL stiffness or EHL spring, is simply the inverse of this flexibility.

Adding forces due to the inertia of the system, the model allows one to construct a simulation by which the damping, induced by the viscous losses in the lubricant, can be determined. In this experiment, the rolling element is slightly lifted (or given an initial velocity) from its equilibrium position and subsequently released. This causes the rolling element to start a damped

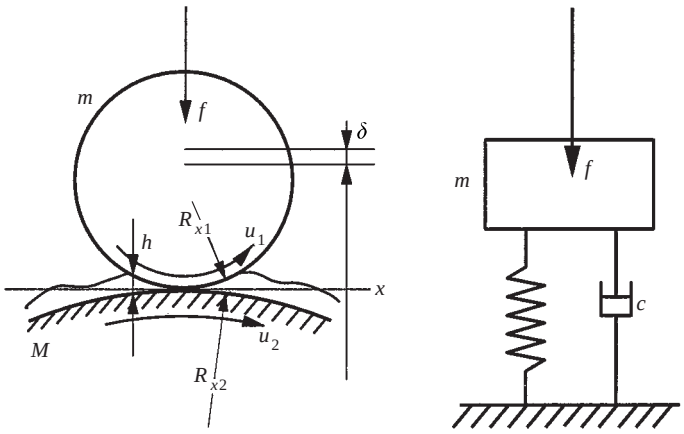

Figure 2. Rolling element on raceway and the approximated spring–damper model.

oscillatory motion around the equilibrium approach. Comparison between the obtained solution and the solution of a simplified model where the rolling element is connected to the raceway by the EHL spring and a linear viscous damper, see Figure 2, yields a value of the damping *constant* for which both solutions are closest to each other.

3. EQUATIONS

In the present analysis the mathematical model used to solve these EHL contact problems includes Reynolds equation, describing the fluid flow in small gaps, the film thickness equation, Roelands' empirical viscosity–pressure relation [8] and the Dowson and Higginson equation, relating compressibility to pressure [9]. In the steady state situation the force balance equation was used whereas the equation of motion has been adopted in transient simulations. The reader is referred to reference [1] for an elaborate discussion on the equations used. The equations were scaled by means of the Hertzian contact parameters (contact width/length and mutual approach), i.e., the contact parameters when no lubrication is present in the gap between the surfaces. All the Hertzian contact parameters that were used are defined in Appendix B.

The dimensionless Reynolds equation reads:

$$\frac{\partial}{\partial X}\left(\frac{\bar{\rho}H^3}{\bar{\eta}\lambda}\frac{\partial P}{\partial X}\right)+\kappa^2\frac{\partial}{\partial Y}\left(\frac{\bar{\rho}H^3}{\bar{\eta}\lambda}\frac{\partial P}{\partial Y}\right)-\frac{\partial(\bar{\rho}H)}{\partial X}-\frac{\partial(\bar{\rho}H)}{\partial T}=0, \tag{1}$$

where λ is the dimensionless parameter:

$$\lambda=\frac{6u_s\eta_0(2R)^2}{a^3p_h}\left(\frac{\mathcal{E}}{\mathcal{K}}\right)^2, \tag{2}$$

where $\mathcal{K}=\mathcal{K}(1-\kappa^2)$ and $\mathcal{E}=\mathcal{E}(1-\kappa^2)$ denote the complete elliptic integrals of the first and second kind, respectively. The dimensionless film thickness is:

$$H(X,\,Y,\,T)=-\Delta+\frac{\mathcal{E}-\kappa^2\mathcal{K}}{\mathcal{K}-\kappa^2\mathcal{K}}X^2+\frac{\mathcal{K}-\mathcal{E}}{\mathcal{K}-\kappa^2\mathcal{K}}Y^2,$$
$$+\frac{1}{\pi\mathcal{K}}\int_S\frac{P(X',\,Y',\,T)\,\mathrm{d}X'\,\mathrm{d}Y'}{\sqrt{\kappa^2(X-X')^2+(Y-Y')^2}}, \tag{3}$$

where Δ is the mutual approach of two remote points in the bodies, the second and third term are the undeformed geometry and the integral term represents the elastic deformation. Finally, the equation of motion reads:

$$\frac{1}{\Omega^2}\frac{\mathrm{d}^2\Delta}{\mathrm{d}T^2}+\frac{3}{2\pi}\int_S P(X',\,Y',\,T)\,\mathrm{d}X'\,\mathrm{d}Y'=1, \tag{4}$$

where Ω is the dimensionless frequency defined by:

$$\Omega^2 = \frac{8fR}{mu_s^2}\frac{\mathcal{E}}{\mathcal{K}}. \tag{5}$$

It is noted that in the steady state situation, the equation of motion reduces to the force balance equation, i.e., the first term in equation (4) vanishes. Roelands' equation, assuming $z = 0{\cdot}67$, adds the parameter $\bar{\alpha}$ to the set of parameters. The total number of variables then becomes four, i.e., the parameters λ, $\bar{\alpha}$, κ and, for the transient model, Ω. For historic reasons, results will be presented in terms of a different set of independent parameters, i.e., the load parameter M and lubricant parameter L. They can be shown to depend on λ and $\bar{\alpha}$.*

4. RESULTS

The equations, given in the previous section, were discretized using a second order scheme with respect to both space and time and subsequently solved; see reference [7]. Multilevel techniques, as described in reference [1], were used to accelerate convergence and for the fast evaluation of the deformation integral. The multilevel integration technique was modified for elliptical contacts.

For small values of M the pressure build-up starts further upstream. Hence, at these small values, the computational domain was increased to avoid so called numerical starvation. The domain was covered by a grid having 257×257 points for all steady state computations, whereas 128×128 points were used in the transient ones.

In this section, the stiffness of the EHL contact for $\kappa = 1{\cdot}0$, $0{\cdot}22$ and $0{\cdot}05$ will be presented for a variety of values of M and L. Approximate relations are derived to obtain the stiffness for intermediate values. As mentioned in the introduction, damping values and its approximate relation, will only be presented for the circular contact case.

4.1. STIFFNESS

Figure 3 shows a typical example of the pressure and film thickness in a steady state EHL, contact. The film thickness is roughly constant in the center of the contact and a constriction can be observed near the outlet. The pressure distribution is approximately Hertzian except near the inlet. Moreover, a second pressure maximum can be observed near the outlet constriction.

For the circular contact, Figure 4 shows Δ_∞ for a number of values of M and L (the subscript ∞ has been added to indicate the approach at equilibrium). From the figure one observes that Δ_∞ goes to unity for large values of M, thus the approach is Hertzian at these values and it is legitimate to approximate the stiffness of the contact by the Hertzian stiffness, i.e., $f \sim \delta^{3/2}$. However, Δ_∞ decreases with M and becomes negative, especially at larger values of L, showing that in this case the stiffness of the lubricant can not be neglected.

$$*\bar{\alpha} = \frac{L}{\pi}\left(\frac{3M}{2}\right)^{1/3}\left(\frac{\pi^2(1+D)^2\kappa}{16\mathcal{E}^2}\right)^{1/3};\ \lambda = \left(\frac{128\pi^3}{3M^4}\right)^{1/3}\left(\frac{16\pi\mathcal{E}^5}{\kappa^4\mathcal{K}^6(1+D)^5}\right)^{1/3}.$$

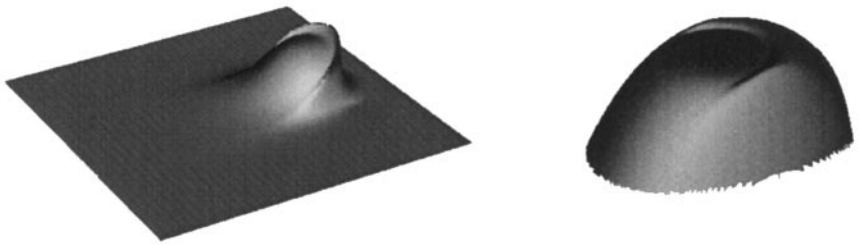

Figure 3. Pressure and film thickness. $M = 250$, $L = 10$ and $\kappa = 0{\cdot}05$. Direction of flow is from left to right.

The results obtained for $\kappa = 0{\cdot}22$ and $\kappa = 0{\cdot}05$ show that this effect becomes stronger for smaller values of κ, i.e., the lubricant's stiffness becomes more important at higher load numbers, see Appendix A.

Assuming that Δ_∞ is of the form $(1 - pM^q)$ and fitting p and q for different values of L, the following curve-fit has been found that closely approximates the computed values:

$$\Delta_\infty(M, L) = 1 - p(L)M^{q(L)} \quad \text{where}$$

$$p(L) = ((4 - 0{\cdot}2L)^7 + (3{\cdot}5 + 0{\cdot}1L)^7)^{1/7} \quad \text{and}$$

$$q(L) = -(0{\cdot}6 + 0{\cdot}6(L + 3)^{-1/2}). \tag{6}$$

The function is shown by the solid line in Figure 4.

From the definition of Δ, the actual approach δ follows from:

$$\delta_\infty = \Delta_\infty(M(f, \ldots), L(\ldots))\left(\frac{9f^2}{8E'^2R}\frac{4\kappa^2\mathcal{K}^3}{\pi^2\mathcal{E}}\right)^{1/3}, \tag{7}$$

where Δ_∞ (M,L) is defined according to equation (6).

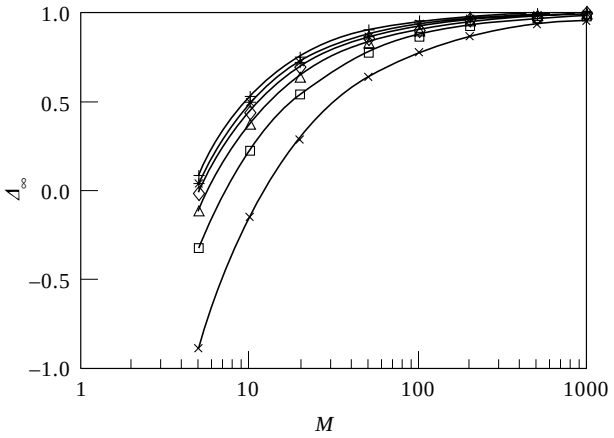

Figure 4. Δ_∞ for different values of M and L and the aproximate relation equation (6). +, $L = 0{\cdot}0$; *, $L = 1{\cdot}0$; ◇, $L = 2{\cdot}5$; △, $L = 5{\cdot}0$; □, $L = 10$; ×, $L = 25$.

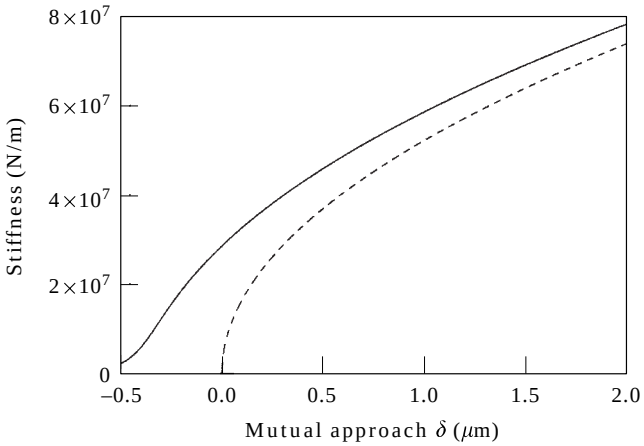

Figure 5. Inner ring stiffness for $\kappa = 0{\cdot}05$ and $L = 10$. —, EHL contact; - - -, dry contact.

Thus, for any approach, given the parameters' speed, radius of curvature, reduced elasticity modulus, viscosity and viscosity index of the lubricant, the load f is given implicitly by equation (7). Since this function is very smooth, it can easily be solved using modified Newton Raphson iteration. As an example, the resulting inner contact stiffness and the Hertzian stiffness is given in Figure 5 for some particular values of the viscosity, rolling speed etc. (Note that in this case L is constant.) The figure shows that at small and negative approaches, the stiffness of the lubricant completely dominates the stiffness.

4.2. DAMPING

The transient simulation, as described in section 2, has been carried out for a number of parameters M and L, for $\kappa = 1{\cdot}0$, i.e., circular contact. In the present work, damping values will be presented for one value of the dimensionless frequency Ω only, i.e., $\Omega = 5{\cdot}13$. At $\Omega = 5{\cdot}13$, one oscillation of the rolling element takes approximately one time unit; see reference [7].

Figure 6 shows an example of the pressure and film thickness at one particular moment in the transient simulation. One clearly observes fluctuations in film thickness and pressure. These fluctuations are explained by the absence of pressure-induced flow in the high pressure region. Neglecting this flow, the Reynolds equation reduces to the advection equation $-\bar{\rho}H_X - \bar{\rho}H_T = 0$. Its solution, $\bar{\rho}H = \bar{\rho}H(X - T)$, indicates that any variation of the film thickness induced at the inlet is propagated through the high pressure zone virtually undisturbed. In the present simulation, the modulations in the inlet region result from the oscillating rolling element, but the same phenomenon has been observed in both numerical and experimental studies on waviness and dents/bumps. Because Ω is proportional to the time a fluid particle needs to pass through the contact region, the wavelength of the film thickness modulations is determined by its value; see reference [7] for a more detailed discussion. Here,

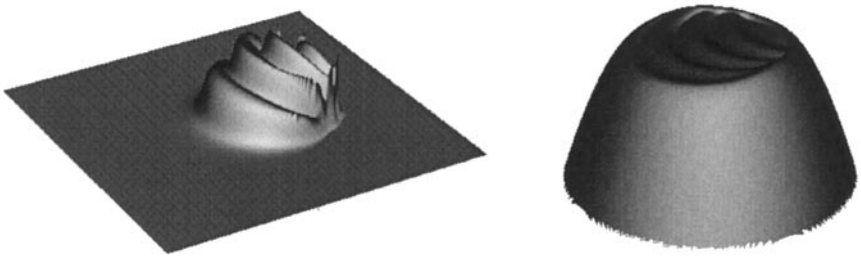

Figure 6. Pressure and film thickness in the transient simulation. $M = 200$, $L = 10$, $\Omega = 10$ and $\kappa = 1{\cdot}0$. The direction of flow is from left to right.

emphasis is on the influence of the lubricant on the oscillating rolling element's center of gravity.

The solid line in Figure 7 shows Δ as a function of time in a simulation for $M = 200$, $L = 10$, $\Omega = 2{\cdot}5$ and $\kappa = 1{\cdot}0$. It shows that, as explained before, the lubricant damps any oscillation as a result of a small deviation from the equilibrium position.

As a next step, this transient response will be characterized by comparison with the EHL spring, defined before, and a linear viscous damper, i.e., the values of the damping constant C will be obtained for which the response, given in Figure 7, is closest, in a least squares sense, to the response of a rolling element connected to the raceway by an EHL spring and linear viscous damper, as was depicted in Figure 2.

The second order differential equation describing the EHL spring–damper model reads:

$$\frac{1}{\Omega^2}\frac{\mathrm{d}^2\Delta}{\mathrm{d}T^2} + C\frac{\mathrm{d}\Delta}{\mathrm{d}T} + \mathcal{I}(\Delta) = 1, \tag{8}$$

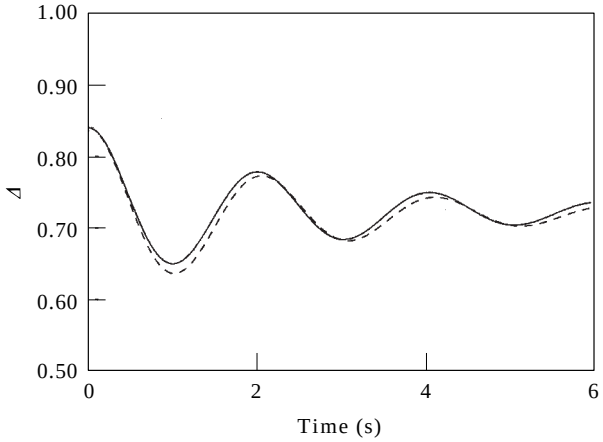

Figure 7. Transient response for $M = 200$, $L = 10$, $\Omega = 2{\cdot}5$ and $\kappa = 1{\cdot}0$. —, EHL; ---, spring–damper.

where C is the dimensionless damping constant defined by

$$C = c\frac{au_s}{4fR}\frac{\mathcal{K}}{\mathcal{E}}. \tag{9}$$

$\mathcal{I}(\Delta)$ is the contact force, obtained from the EHL spring in dimensionless variables:

$$\Delta = \Delta_\infty(\mathcal{I}M, L)(\mathcal{I})^{2/3}. \tag{10}$$

Since the load was only given implicitly, $\mathcal{I}(\delta)$ has been introduced to formally describe the explicit relation between approach and contact force. Only in the case of equilibrium is the contact force equal to the applied load, i.e., $\mathcal{I}(\Delta_\infty) = 1$. For constant C, the solution of equation (8) can easily be obtained using the Newmark integration scheme combined with Newton Raphson iteration to calculate the force due to the EHL spring.

The response of the EHL spring–damper model for $M = 200$, $L = 10$, $\Omega = 2{\cdot}5$ and $\kappa = 1$ is plotted by the dashed line in Figure 7. The damping for which the response was closest to the calculated response was $C \approx 0{\cdot}005$. For different values of M and L and $\kappa = 1{\cdot}0$, Figure 8 shows C obtained in the way described before. As can be observed, the damping decreases with M and L. This can be explained by the "boundary layer" that exists just upstream of the Hertzian contact region. It can be shown that viscous losses predominantly occur inside this layer and because it decreases for increasing M and L, damping decreases as well.

To obtain the damping constant for intermediate values of M and L, the following curve-fit provides a convenient approximation:

$$\begin{aligned} C(M, L) &= r(L)M^{s(L)} \quad \text{where} \\ r(L) &= 0{\cdot}98 - L/60 \quad \text{and} \\ s(L) &= -0{\cdot}83 - L/125. \end{aligned} \tag{11}$$

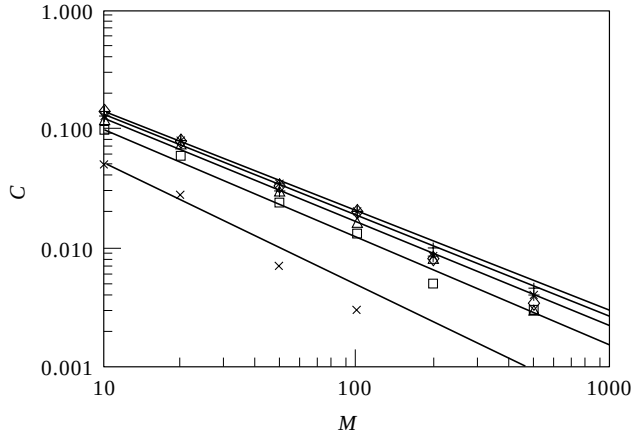

Figure 8. C for different values of M and L and the approximated equation (11). +, $L = 0{\cdot}0$; *, $L = 1{\cdot}0$; ◇, $L = 2{\cdot}5$; △, $L = 5{\cdot}0$; □, $L = 10$; ×, $L = 25$.

Numerical experiments show that the damping increases with decreasing ellipticity. Despite the present second order discretization and the fine mesh that is used, the discretization error is still large for very small ellipticity ratios, i.e., $\kappa \leqslant 0{\cdot}1$. This error manifests itself in an increase in damping, hence it is generally referred to as numerical damping. Because the physical damping becomes comparable to the numerical damping, no quantitative data will be presented for elliptical contacts.

5. THE STRUCTURAL DYNAMICS MODEL

A frictionless non-linear dynamic model is developed that describes the interaction between the different structural components of a ball bearing, i.e., the inner ring, the outer ring and the rolling elements. Except for the local contact deformations, the inner ring is modelled as a rigid body having six degrees of freedom. However, the rotational velocity around the bearing axis of symmetry is assumed to be constant. This leaves only five degrees of freedom for the inner ring. If it is desired, the inner ring can be coupled to a flexible shaft. However, for the particular example in this paper, the shaft is assumed to be rigidly connected to the world. This assumption is allowed because the outer ring can move freely. The result is that all the inner ring co-ordinates are prescribed and do not constitute part of the solution.

The rolling elements are modelled as point masses having only two degrees of freedom each, a radial and an axial displacement co-ordinate. The tangential co-ordinate of the qth rolling element is prescribed by the angular cage speed according to

$$\theta_q = \omega_m t + (q-1)\Delta\theta, \tag{12}$$

where $\Delta\theta = 2\pi/Z$ and Z is the number of rolling elements. In case pure rolling is assumed in the contacts, ω_m is related to the angular shaft speed ω_i by

$$\omega_m = \frac{\omega_i}{2}\left\{1 - \frac{D\cos(\alpha)}{d_m}\right\}. \tag{13}$$

The cage separates the rolling elements and prevents them from sliding against each other. Cage forces are assumed to be small compared to the contact forces between the rolling elements and the raceway. The function of the cage is accounted for by assuming a constant pitch velocity for each rolling element.

Unlike the inner ring, the outer ring is modelled as a flexible body using finite element techniques. The applied finite element model is given in Figure 9. If it is desired, a flexible housing can be added to the outer ring resulting in a single FEM model for the outer ring and the bearing housing. In that case an ideal outer ring housing interface is assumed (see reference [10]). For an accurate description of the outer ring a large number of elements is required resulting in unacceptably long computation times in the case of transient calculations. A component mode synthesis technique (CMS) is introduced to reduce the number of degrees of freedom. The CMS technique, which is based on the Ritz assumed deflection method, describes the discetized displacement field of the outer ring

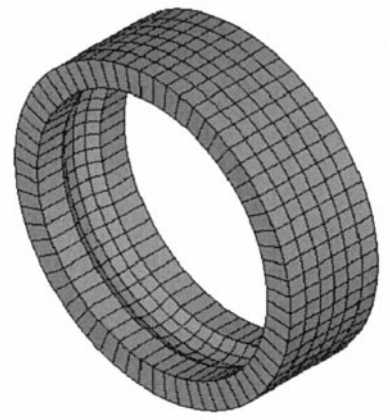

Figure 9. Finite element model used for the outer ring.

with a series of suitable shape functions, also referred to as the generalized co-ordinates

$$u(x_j, t) = \sum_{i=1}^{N} \Psi_i(x_j) p_i(t) = [\mathbf{\Psi}_j]\{\mathbf{p}\}. \tag{14}$$

The reduced mass and stiffness matrices are then obtained by

$$[\mathbf{m}] = [\mathbf{\Psi}_j]^T[\mathbf{m}_j][\mathbf{\Psi}_j], \qquad [\mathbf{k}] = [\mathbf{\Psi}_j]^T[\mathbf{k}_j][\mathbf{\Psi}_j]. \tag{15, 16}$$

The reduced system must still give an accurate description of the mode shapes in the frequency range of interest. Furthermore, it must be able to describe the static solution and fulfill the boundary conditions. It is obvious that natural mode shapes alone do not fulfill these requirements. In the literature several techniques have been developed, such as the Craig–Bampton method and the method of reduced flexibilities. However, for several reasons, these techniques are not directly applicable to the bearing problem. First of all, neither technique can describe the effect of moving loads, because the interface nodes are fixed. Secondly, the discrete description of the shape functions gives rise to undesired artificial impact phenomena.

A new CMS technique is introduced, based on the Craig–Bampton method in the sense that it also uses fixed normal modes and (redundant) constraint modes but, instead of using a number of unit displacement functions, it uses a series of analytical functions for the interface nodes. The reason for using constraint modes instead of flexibility modes is the efficient coupling procedure. For a bearing this is very important regarding the many ball raceway contacts.

It is assumed that all points on the raceway can come into contact with the rolling elements and that the contact forces are always directed normal to the raceway surface. This means that every node on the raceway can be regarded as an interface node and that analytical functions are required for the radial and axial displacement field on the raceway. In the present study, the displacements of the raceway in the circumferential direction are described by Fourier series

whereas for the axial displacements Chebyshev polynomials were used:

$$u_r = \sum_{n=0}^{N_f}\sum_{m=0}^{N_c} a_r \cos(n\theta)\cos\left(m\arccos\left(\frac{z}{z_0}\right)\right) + \sum_{n=1}^{N_f}\sum_{m=0}^{N_c} b_r \sin(n\theta)\cos\left(m\arccos\left(\frac{z}{z_0}\right)\right), \tag{17}$$

$$u_z = \sum_{n=0}^{N_f}\sum_{m=0}^{N_c} a_z \cos(n\theta)\cos\left(m\arccos\left(\frac{r}{r_0}\right)\right) + \sum_{n=1}^{N_f}\sum_{m=0}^{N_c} b_z \sin(n\theta)\cos\left(m\arccos\left(\frac{r}{r_0}\right)\right). \tag{18}$$

An important feature of these series is that they are able to describe both rigid body translations and rotations, as well as twisting of the outer ring. With the present technique, the FEM model with.several thousands of degrees of freedom is reduced to a model with approximately 100 degrees of freedom.

Together with the equations for the stiffness and damping, as derived in section (2), one can construct the Lagrangian equations of motion for the bearing outer ring:

$$[\mathbf{m}]\{\ddot{\mathbf{q}}\} + [\mathbf{k}]\{\mathbf{q}\} + \sum_{s=1}^{Q} F_{sor}\frac{\partial F_{sor}}{\partial q} + \sum_{s=1}^{Q} F_{sor}\frac{\partial F_{sor}}{\partial \dot{q}} = \{\mathbf{F}\}. \tag{19}$$

The equation of motion for the rolling elements read:

$$m\ddot{v}_s + F_{sor}\frac{\partial F_{sor}}{\partial v_s} + F_{sir}\frac{\partial F_{sir}}{\partial v_s} + F_{sor}\frac{\partial F_{sor}}{\partial \dot{v}_s} + F_{sir}\frac{\partial F_{sir}}{\partial \dot{v}_s} = \frac{1}{2}m_{re}\omega_m^2 d_m, \tag{20}$$

$$m\ddot{w}_s + F_{sor}\frac{\partial F_{sor}}{\partial w_s} + F_{sir}\frac{\partial F_{sir}}{\partial w_s} + F_{sor}\frac{\partial F_{sor}}{\partial \dot{w}_s} + F_{sir}\frac{\partial F_{sir}}{\partial \dot{w}_s} = 0, \tag{21}$$

for $s = 1 \ldots Q$. In the above equations, F_{sir} and F_{sor} contain both restoring and dissipative forces. The equations of motion are integrated by means of the Newmark time integration method in combination with a modified Newton Raphson iteration. A fast implementation is possible, making use of analytical approximations to the contact forces.

6. RESULTS

6.1. BEARING EIGENFREQUENCIES

The geometry of the bearing used for this numerical study resembles a DGBB 6202, i.e., eight rolling elements, a 35-mm outer bore and a 15-mm inner bore. The bearing is subjected to a pure axial load. Because of this preload, the initial

TABLE 1
Eigenfrequencies of a non-rotating DGBB 6202, $F_z = 60$ N

No.	Frequency (kHz)	Mode shape
1,2	0·8	Tilting mode
3	3·3	Axial mode
4,5	9·0	Radial mode
6,7	11·8	Flexural mode out of plane
8,9	12·7	Flexural mode in plane

clearance vanishes and all rolling elements are in contact with the raceways. The static equilibrium is determined to obtain the mean stiffness matrix. Together with the mass matrix, the eigenfrequencies and mode shapes of the undamped non-rotating bearing system can be calculated; see Table 1. In the present study, focus will be on the bearing outer ring modes.

In the case of a non-rotating bearing, the EHL contacts behave as dry contacts. Once the bearing rotates, a sum speed is created and a fluid film is built up between the rolling elements and the raceway. This film influences the stiffness and thus the eigenfrequencies of the bearing. Obviously, in the case of a dry contact model the eigenfrequencies are independent of the rotational speed. In Figure 10 the different bearing eigenfrequencies are plotted against the rotational speed. The eigenfrequencies are scaled on the dry contact situation. The following lubrication parameters are used: the pressure–viscosity coefficient $\alpha = 1{\cdot}0 \times 10^{-8}$ Pa^{-1} and the viscosity at room temperature $\eta_0 = 0{\cdot}1$ Pa s.

It is observed that all the eigenfrequencies increase, except for the eigenfrequency of the axial mode shape. An increase in the eigenfrequency could be explained by the stiffening effect of the lubricant. However, this does not explain the decrease in eigenfrequency of the axial mode. To understand this effect, the contact angle and contact force are plotted against the rotational speed in Figures 11 and 12, respectively.

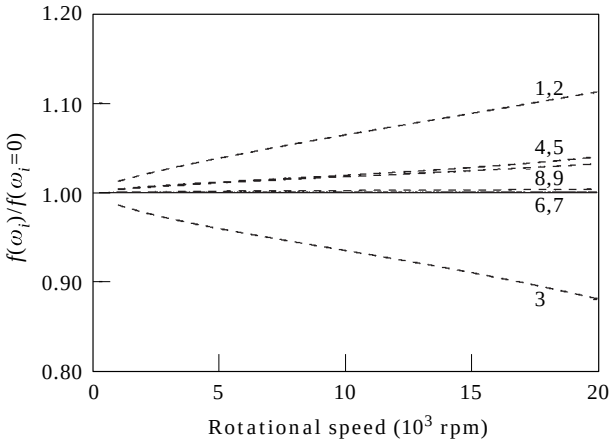

Figure 10. Effect of rotational speed on the bearing eigenfrequencies.

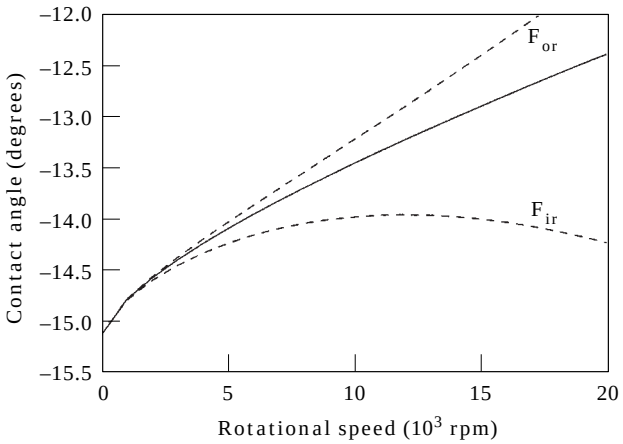

Figure 11. Effect of rotational speed on the contact angle. —, No centrifugal effect; – – –, centrifugal effect.

Because of the increasing film that is built up in the contact, the contact forces increase. However, in the axial direction equilibrium must be maintained with the applied external force. The only way out for the bearing is to adjust the contact angles. The bearing stiffness heavily depends on the angle of contact. When the contact angle decreases, the radial stiffness component increases and the axial stiffness component decreases. It is concluded that this effect must be much stronger than the stiffening effect due to higher contact loads. An increase in the first bearing eigenfrequency as a function of the rotational speed has also been found experimentally by Dietl and Zeillinger [11].

6.2. MODAL DAMPING

To estimate modal damping coefficients, transfer functions of the bearing have to be determined. The most effective way to do so, is to apply a random force on

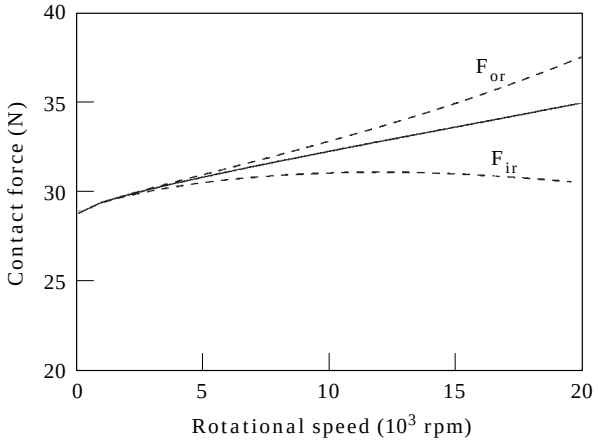

Figure 12. Effect of rotational speed on the contact force. —, No centrifugal effect; – – –, centrifugal effect.

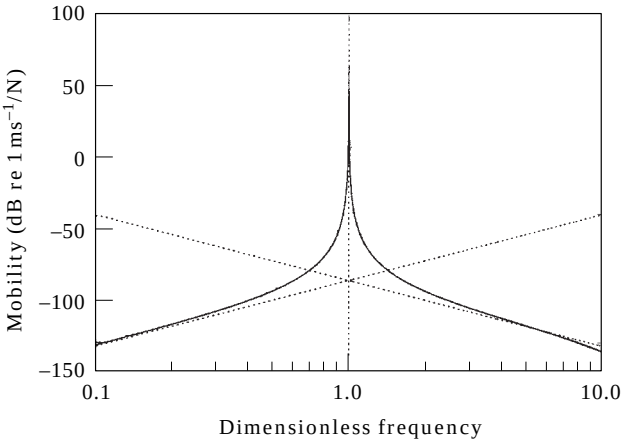

Figure 13. Mobility function first mode DGBB 6202.

the system. In this numerical example, the random force is applied at one rolling element. The calculated time signal of the generalized co-ordinates is then transformed into the natural co-ordinates of the bearing. Each co-ordinate now represents a single degree of freedom. In Figure 13, the mobility of the first tilting mode is depicted.

The damping is estimated by analyzing the real part of the complex transfer functions. Near the resonance frequency the real part has a maximum at ω_1 and a minimum at ω_2. The EHL model assumes viscous damping and the viscous damping coefficient estimated from EHL calculations equals 100 N s/m. The bearing is loaded with an axial force of 100 N. The dimensionless viscous damping coefficient is given by

$$2\zeta = \frac{(\omega_1/\omega_2)^2 - 1}{(\omega_1/\omega_2)^2 + 1}. \tag{22}$$

The dimensionless viscous damping coefficient ζ of each mode is presented in Table 2.

TABLE 2

Modal damping coefficients DGBB 6202, $F_z = 100$ N

No.	Frequency (kHz)	Mode shape	ζ
1,2	1·0	Tilting mode	0·001
3	3·8	Axial mode	0·02
4,5	9·8	Radial mode	0·06
6,7	11·8	Flexural mode out of plane	0·01
8,9	13·6	Flexural mode in plane	0·07

7. CONCLUSION

The stiffness and damping of an elliptical EHL contact have been obtained for a wide variety of load and lubricant parameters using fast and efficient numerical algorithms and have been approximated by analytical relations. The incorporation of these relations into a structural dynamics model, that incorporates a flexible outer ring, proved to work quite well. It captures the major influence of the lubricant on the dynamic behaviour of the complete bearing. This influence, as compared to the dry contact situation, is moderate for medium loads and low rotational speeds but increases for low loads and higher speeds. From the simulations, it is observed that the eigenfrequencies of a lubricated bearing shift as a result of the decreased contact angles. Moreover, the mobility functions show large differences in modal damping at the different bearing resonances. The tilting modes, for instance, are only slightly damped, indicating that other sources of damping which are not incorporated in the model might become more important.

ACKNOWLEDGMENT

The authors wish to thank Professor H. Tijdeman and C. H. Venner for their valuable contributions and encouraging interest. Furthermore, the authors gratefully acknowledge the support of the SKF Engineering & Research Centre B.V., Nieuwegein, The Netherlands.

REFERENCES

1. C. H. VENNER 1991 *PhD Thesis*, *University of Twente*, *Enschede*, *The Netherlands*. ISBN 90-9003974-0. Multilevel solution of the EHL line and point contact problems.
2. C. H. VENNER and A. A. LUBRECHT 1994 *ASME Journal of Tribology* **116**, 751–761. Numerical simulation of a transverse ridge in a circular EHL contact, under rolling/sliding.
3. C. H. VENNER and A. A. LUBRECHT 1995 *ASME Journal of Tribology* **118**, 153–161. Numerical analysis of influence of waviness on the film thickness of a circular EHL contact.
4. P. R. YANG and S. Z. WENG 1991 *WEAR* **142**, 1–16, 17–30. Pure squeeze action in an isothermal elastohydrodynamically lubricated spherical conjunction. Parts 1 and 2.
5. R. LARSSON 1996 *Doctoral Thesis*, *Luleå University of Technology*, *Sweden*. ISSN 0348-8373. Elastohydrodynamic lubrication under non-steady conditions.
6. D. DOWSON and D. WANG 1995 *Proceedings of the* 21*st Leeds Lyon Symposium on Tribology*, 565–582. Impact elastohydrodynamics.
7. Y. H. WIJNANT and C. H. VENNER 1996 *Proceedings of the* 23*rd Leeds Lyon Symposium on Tribology*. Analysis of an EHL circular contact incorporating rolling element vibration.
8. C. J. A. ROELANDS 1966 *PhD Thesis*, *Technische Hogeschool Delft*, *The Netherlands* (V.R.B., Groningen, The Netherlands). Correlational aspects of the viscosity–temperature–pressure relationship of lubricating oils.
9. D. DOWSON and G. R. HIGGINSON 1966 *Elasto-hydrodynamic Lubrication*, *The Fundamentals of Roller and Gear Lubrication*. Oxford: Pergamon Press.

10. J. A. WENSING and G. C. VAN NIJEN 1996 *Proceedings of the 6th International Conference on Vibrations in Rotating Machinery*, IMechE, 371–382. 2-dimensional computational model for vibrations analysis of waviness in rolling bearing applications.
11. P. DIETL and R. ZEILLINGER 1997 *Schwingungen in Rotierenden Machinen* **IV**, 3–10. Zur Dämpfung in Wälzlagerungen—Theorie und Experiment, Vieweg, Braunschweig, ISBN 3528069082.

APPENDIX A: APPROACH IN ELLIPTICAL CONTACTS

Similar to the circular contact, the dimensionless approach Δ_∞ has been approximated by $1 - p(L)M^{q(L)}$ where, for $\kappa = 0{\cdot}22$:

$$p(L) = ((13{\cdot}6 - 0{\cdot}6L)^5 + (10 + 0{\cdot}14L)^5)^{1/5}, \tag{23}$$

$$q(L) = -((0{\cdot}19 + (0{\cdot}88 - 0{\cdot}028L)^5))^{1/5}, \tag{24}$$

and for $\kappa = 0{\cdot}05$

$$p(L) = 47{\cdot}6 - 3{\cdot}35L + 0{\cdot}20L^2 - 0{\cdot}0036L^3, \tag{25}$$

$$q(L) = -((0{\cdot}752 - 0{\cdot}04L + 0{\cdot}0005L^2))^3 + (0{\cdot}8 - 0{\cdot}002L)^3)^{1/3}. \tag{26}$$

To obtain the dimensionless approach for intermediate values of κ, interpolation between equation (6) and the equations given above may be carried out.

APPENDIX B: NOMENCLATURE

a	Hertzian contact length	$a = (3fR/E')^{1/3}(2\kappa\mathcal{E}/\pi)^{1/3}$
$a_{r,z}$	amplitudes Fourier/Chebyshev series	
b	Hertzian contact width	$b = a/\kappa$
c	Hertzian approach	$c = (a^2/(2R))(\mathcal{K}/\mathcal{E})$
c	damping constant	
C	dimensionless damping	$C = c(au_s/4fR)(\mathcal{K}/\mathcal{E})$
E'	reduced modulus of elasticity	$2/E' = \frac{1-\nu_1^2}{E_1} + \frac{1-\nu_2^2}{E_2}$
d_m	rolling element diameter	
D	diameter bearing	
f	load	
F_{or}	outer ring load	
F_{ir}	inner ring load	
F_z	axial load	
H	dimensionless film thickness	$H = h(2R/a^2)(\mathcal{E}/\mathcal{K})$
k	stiffness	
[**k**]	stiffness matrix	
L	dimensionless lubricant parameter	$L = \alpha E'\left(\frac{\eta_0 u_s}{E' R_x}\right)^{1/4}$
m	mass rolling element	

$[\mathbf{m}]$	mass matrix	
M	dimensionless load parameter	$M = \dfrac{f}{E' R_x^2}\left(\dfrac{E' R_x}{\eta_0 u_s}\right)^{3/4}$
p	pressure	
p_h	maximum Hertzian pressure	$p_h = 3f/(2\pi ab)$
P	dimensionless pressure	$P = p/p_h$
q	displacements outer ring	
R	reduced radius of curvature	$R^{-1} = R_x^{-1} + R_y^{-1}$
R_x	reduced radius of curvature in x-direction	$R_x^{-1} = R_{x1}^{-1} + R_{x2}^{-1}$
R_y	reduced radius of curvature in y-direction	$R_y^{-1} = R_{y1}^{-1} + R_{y2}^{-1}$
S	computational domain	
t	time	
T	dimensionless time	$T = tu_s/(2a)$
u	displacement field	
u_s	sum velocity	$u_s = u_1 + u_2$
v	displacement rolling element (radial)	
w	displacement rolling element (axial)	
x	co-ordinate in direction of flow	
X	dimensionless co-ordinate	$X = x/a$
y	co-ordinate perpendicula to x	
Y	dimensionless co-ordinate	$Y = y/b$
z	pressure viscosity parameter (Roelands)	
α	pressure viscosity index	
α	contact angle	
$\bar{\alpha}$	dimensionless viscosity parameter	$\bar{\alpha} = \alpha p_h$
δ	mutual approach	
Δ	dimensionless mutual approach	$\Delta = \delta(2R/a^2)(\mathcal{E}/\mathcal{K})$
η	viscosity	
η_0	viscosity at ambient pressure	
$\bar{\eta}$	dimensionless viscosity	$\bar{\eta} = \eta/\eta_0$
ζ	viscous damping	
θ_q	tangential co-ordinate of roller q	
$\boldsymbol{\Psi}$	generalized co-ordinates	
κ	ellipticity ratio	$\kappa = a/b$
λ	dimensionless speed parameter	$\lambda = \dfrac{6\eta_0 u_s (2R)^2}{a^3 p_h}\left(\dfrac{\mathcal{E}}{\mathcal{K}}\right)^2$
$\nu_{1,2}$	Poisson's ratio body 1,2	
ρ	density	
ρ_0	density at ambient pressure	
$\bar{\rho}$	dimensionless density	$\bar{\rho} = \rho/\rho_0$
ω_n	cage speed	
ω_i	shaft speed	
$\omega_{1,2}$	eigenfrequencies	
Ω	dimensionless frequency	$\Omega^2 = (8fR/(mu_s^2))(\mathcal{E}/\mathcal{K})$
$\mathcal{K}$	elliptic integral of the first kind	
$\mathcal{E}$	elliptic integral of the second kind	